

# Measurement of Strain in the Left Ventricle during Diastole with cine-MRI and Deformable Image Registration

**Alexander I. Veress**

Department of Bioengineering, and Scientific Computing and Imaging Institute, University of Utah, Salt Lake City, UT

**Grant T. Gullberg**

E. O. Lawrence Berkeley National Laboratory, Berkeley, CA

**Jeffrey A. Weiss<sup>1</sup>**

Department of Bioengineering, and Scientific Computing and Imaging Institute, University of Utah, 50 South Central Campus Drive, Room 2480, Salt Lake City, Utah 84112-9202  
e-mail: jeff.weiss@utah.edu

*The assessment of regional heart wall motion (local strain) can localize ischemic myocardial disease, evaluate myocardial viability, and identify impaired cardiac function due to hypertrophic or dilated cardiomyopathies. The objectives of this research were to develop and validate a technique known as hyperelastic warping for the measurement of local strains in the left ventricle from clinical cine-magnetic resonance imaging (MRI) image datasets. The technique uses differences in image intensities between template (reference) and target (loaded) image datasets to generate a body force that deforms a finite element (FE) representation of the template so that it registers with the target image. To validate the technique, MRI image datasets representing two deformation states of a left ventricle were created such that the deformation map between the states represented in the images was known. A beginning diastolic cine-MRI image dataset from a normal human subject was defined as the template. A second image dataset (target) was created by mapping the template image using the deformation results obtained from a forward FE model of diastolic filling. Fiber stretch and strain predictions from hyperelastic warping showed good agreement with those of the forward solution ( $R^2=0.67$  stretch,  $R^2=0.76$  circumferential strain,  $R^2=0.75$  radial strain, and  $R^2=0.70$  in-plane shear). The technique had low sensitivity to changes in material parameters ( $\Delta R^2=-0.023$  fiber stretch,  $\Delta R^2=-0.020$  circumferential strain,  $\Delta R^2=-0.005$  radial strain, and  $\Delta R^2=0.0125$  shear strain with little or no change in rms error), with the exception of changes in bulk modulus of the material. The use of an isotropic hyperelastic constitutive model in the warping analyses degraded the predictions of fiber stretch. Results were unaffected by simulated noise down to a signal-to-noise ratio (SNR) of 4.0 ( $\Delta R^2=-0.032$  fiber stretch,  $\Delta R^2=-0.023$  circumferential strain,  $\Delta R^2=-0.04$  radial strain, and  $\Delta R^2=0.0211$  shear strain with little or no increase in rms error). This study demonstrates that warping in conjunction with cine-MRI imaging can be used to determine local ventricular strains during diastole. [DOI: 10.1115/1.2073677]*

*Keywords: Strain, Left ventricle, Deformable image registration, Soft tissue mechanics, Finite element, Magnetic resonance imaging*

## 1 Introduction

Left ventricular (LV) wall function is typically evaluated by the measurement of global measures of ventricular deformation such as ejection fraction, and by local estimates of wall deformation such as wall motion and wall thickening. Techniques that have been employed include two-dimensional (2D) Doppler echocardiography [1,2], cine-magnetic resonance imaging (MRI) [3], and radionuclide ventriculography [4]. Global measures of ventricular function such as ejection fraction do not provide information on the location of functional deficits. Wall motion and wall thickening analyses provide useful local measures of wall function but are at best an indirect measure of local tissue contraction and dilation.

The measurement of local wall deformation (strain) or fiber contraction and/or extension (stretch) can provide insight into local myocardial pathologies such as ischemia. While tagged MRI can measure local deformation [5], fiber stretch cannot be determined without a model representing the mechanics of the myocar-

dium [6]. Similarly, displacement measurements made by tracking the epi- and endocardial surfaces with cine-MRI have been combined with an anisotropic linear elasticity model to estimate fiber stretch and myocardial strain [7]. However, myocardial tissue is nonlinear and undergoes finite deformation [8]. Alternatively, the strain tensor information may be reoriented to the fiber coordinate system. Tseng coregistered diffusion tensor MR (fiber distribution) and strain rate MR to obtain fiber stretch estimates for the mid-ventricle [9]. However, the strain tensor information was based on 2D strain rate measurements and was applied only to the mid-ventricle rather than the entire LV.

Hyperelastic warping, a technique for deformable image registration, allows the determination of local tissue deformation from pairs or sequences of medical image data [10–13]. Deformable image registration techniques determine a deformation map that registers a *template* and *target* image. In hyperelastic warping, a discretized template image is defined as a hyperelastic material governed by nonlinear continuum mechanics. This ensures that mappings from template to target are diffeomorphic (one-to-one, onto, differentiable, and invertible) [14]. The technique has been used to determine strain from sequences of images of deforming tissue without the need for markers [10] or other fiducials such as MR tags, and in theory it can be used with any type of unimodal image data.

<sup>1</sup>Corresponding author.

Contributed by the Bioengineering Division of ASME for publication in the JOURNAL OF BIOMECHANICAL ENGINEERING. Manuscript received December 14, 2004; final manuscript received July 26, 2005. Review conducted by: Andrew D McCulloch.

The objectives of this study were to develop and validate the use of hyperelastic warping for the extraction of high-resolution strain maps of the left ventricle from cine-MRI images. The sensitivity of predictions to errors in material model selection, material parameters, and simulated noise in the image data was determined. The hypotheses were that (i) hyperelastic warping could accurately predict the fiber stretch (ratio of final length to initial length along the local fiber direction) and in-plane strain distributions during diastolic (passive) filling from cine-MRI image datasets, (ii) variations in the assumed material properties and constitutive model would have a minimal effect on the predicted fiber stretch distribution, and (iii) the results of warping cardiac cine-MRI images would be relatively insensitive to noise in the image data.

## 2 Materials and Methods

**2.1 Finite Deformation Theory.** A Lagrangian reference frame is assumed. The template and target images have spatially varying scalar intensity fields, denoted by  $T$  and  $S$ , respectively. The deformation map is  $\varphi(X) = \mathbf{x} = X + \mathbf{u}(X)$ , where  $\mathbf{x}$  are current (deformed) coordinates corresponding to  $X$  (undeformed coordinates) and  $\mathbf{u}(X)$  is the displacement field.  $\mathbf{F}$  is the deformation gradient:

$$\mathbf{F}(X) = \frac{\partial \varphi(X)}{\partial X}. \quad (1)$$

The change in density is related to  $\mathbf{F}$  through the Jacobian,  $J := \det(\mathbf{F}) = \rho_0 / \rho$ , where  $\rho_0$  and  $\rho$  are densities in the reference and deformed configurations, respectively. The positive definite, symmetric left Cauchy-Green deformation tensor is  $\mathbf{C} = \mathbf{F}^T \mathbf{F}$ .

**2.2 Variational Framework for Deformable Image Registration.** Most deformable image registration methods can be posed as the minimization of an energy functional  $E$  with two terms:

$$E(\varphi) = \int_{\beta} W(X, \varphi) \frac{dv}{J} + \int_{\beta} U(T(X, \varphi), S(X, \varphi)) \frac{dv}{J}. \quad (2)$$

$W$  provides regularization and/or some constraint on the deformation map (e.g., one-to-one mapping or no negative volumes), while  $U$  depends on the registration of the template ( $T$ ) and target ( $S$ ) image data.  $\beta$  is the volume of integration in the deformed configuration.

The Euler-Lagrange equations are obtained by taking the first variation of  $E(\varphi)$  with respect to the deformation  $\varphi$  in the direction  $\boldsymbol{\eta}$ , denoted  $\varepsilon \boldsymbol{\eta}$ , where  $\varepsilon$  is an infinitesimal scalar, and then letting  $\varepsilon \rightarrow 0$  [15]. The first variation of the first term in Eq. (2) defines the forces per unit volume from the regularization, while the second term in Eq. (2) gives rise to an image-based force term:

$$G(\varphi, \boldsymbol{\eta}) := DE(\varphi) \cdot \boldsymbol{\eta} = \int_{\beta} \frac{\partial W}{\partial \varphi} \cdot \boldsymbol{\eta} \frac{dv}{J} + \int_{\beta} \frac{\partial U}{\partial \varphi} \cdot \boldsymbol{\eta} \frac{dv}{J} = 0. \quad (3)$$

Equation (3) is a highly nonlinear function of the deformation  $\varphi$ . An incremental-iterative solution method is necessary to obtain the deformation map  $\varphi$  that satisfies the equation. The most common approach is based on Newton's method. Assuming that a solution  $\varphi^*$  is known, a solution is sought at  $\varphi^* + \Delta \mathbf{u}$  where  $\Delta \mathbf{u}$  is a variation in the configuration (virtual displacement). The linearization of Eq. (3) at  $\varphi^*$  in the direction  $\Delta \mathbf{u}$  is defined as

$$L_{\varphi^*} G := G(\varphi^*, \boldsymbol{\eta}) + DG(\varphi^*, \boldsymbol{\eta}) \cdot \Delta \mathbf{u} = \int_{\beta} \boldsymbol{\eta} \cdot \left( \frac{\partial W}{\partial \varphi} + \frac{\partial U}{\partial \varphi} \right) \frac{dv}{J} + \int_{\beta} \boldsymbol{\eta} \cdot (\mathbf{D} + \mathbf{k}) \cdot \Delta \mathbf{u} \frac{dv}{J}, \quad (4)$$

where  $\mathbf{k} := \partial^2 U / \partial \varphi \partial \varphi$  is the image stiffness and  $\mathbf{D} := \partial^2 W / \partial \varphi \partial \varphi$  is the regularization stiffness.

**2.3 Particular Forms for  $W$  and  $U$ —Hyperelastic Warping.** In hyperelastic warping, a spatial discretization of the template image is deformed into alignment with the target image. The target image remains fixed with respect to reference configuration and does not change over the course of the analysis. Assuming that  $T$  is not changed by the deformation it is represented as  $T(X)$ . The values of  $S$  at the material points associated with the deforming template change as the template deforms with respect to the target; it is written as  $S(\varphi)$ . In other words, from the perspective of the material points associated with the template image, the target intensity changes with deformation while the template intensity does not. The standard formulation uses a Gaussian sensor model for the image energy [14]:

$$U(X, \varphi) = \frac{\lambda}{2} [T(X) - S(\varphi)]^2. \quad (5)$$

$\lambda$  is a penalty parameter that enforces alignment of the template model with the target image. As  $\lambda \rightarrow \infty$ ,  $[T(X) - S(\varphi)]^2 \rightarrow 0$ , and the image energy converges to a finite, minimized value.

Hyperelastic warping assumes that  $W$  is the hyperelastic strain energy from continuum mechanics. Since  $W$  depends on  $\mathbf{C}$ , which is independent of rotation, hyperelasticity provides an objective (invariant under rotation) constitutive framework. With these specific assumptions, Eq. (2) takes the form

$$E(\varphi) = \int_{\beta} W(X, \mathbf{C}) \frac{dv}{J} - \int_{\beta} U(T(X), S(\varphi)) \frac{dv}{J}. \quad (6)$$

The first variation of the first term in Eq. (6) yields the weak form of the momentum equations from nonlinear solid mechanics (see, e.g., Ref. [15]). The first variation of the functional  $U$  in Eq. (5) gives rise to the image-based force term

$$DU(X, \varphi) \cdot \boldsymbol{\eta} = -\lambda \left[ [T(X) - S(\varphi)] \frac{\partial S(\varphi)}{\partial \varphi} \cdot \boldsymbol{\eta} \right]. \quad (7)$$

This term drives the template deformation based on pointwise differences in image intensity and the gradient of the target intensity, evaluated at material points in the template model. A similar computation for the term  $W$  leads to the weak form of the momentum equation (see, e.g., Ref. [16]):

$$G(\varphi, \boldsymbol{\eta}) := DE(\varphi) \cdot \boldsymbol{\eta} = \int_{\beta} \boldsymbol{\sigma} : \nabla \boldsymbol{\eta} dv - \int_{\beta} \lambda \left[ (T - S) \frac{\partial S}{\partial \varphi} \cdot \boldsymbol{\eta} \right] \frac{dv}{J} = 0. \quad (8)$$

Here, “:” denotes the tensor inner product and  $\boldsymbol{\sigma}$  is the second-order symmetric Cauchy stress tensor,

$$\boldsymbol{\sigma} = \frac{1}{J} \mathbf{F} \frac{\partial W}{\partial \mathbf{C}} \mathbf{F}^T. \quad (9)$$

Thus the image-based forces are opposed by internal forces, arising from the constitutive model.

The linearization of Eq. (8) at  $\varphi^*$  in the direction  $\Delta \mathbf{u}$  yields

$$L_{\varphi^*} G(\varphi, \boldsymbol{\eta}) = \int_{\beta} \boldsymbol{\sigma} : \nabla \boldsymbol{\eta} dv - \int_{\beta} \lambda \left[ (T-S) \frac{\partial S}{\partial \varphi^*} \cdot \boldsymbol{\eta} \right] \frac{dv}{J} \quad \mathbf{K}^I = \int_{\beta} \mathbf{N}^T \mathbf{k} \mathbf{N} \frac{dv}{J}. \quad (17)$$

$$+ \int_{\beta} \nabla \boldsymbol{\eta} : \boldsymbol{\sigma} : \nabla (\Delta \mathbf{u}) dv + \int_{\beta} \nabla^s \boldsymbol{\eta} : \mathbf{c} : \nabla^s (\Delta \mathbf{u}) dv$$

$$+ \int_{\beta} \boldsymbol{\eta} \cdot \mathbf{k} \cdot \Delta \mathbf{u} \frac{dv}{J} \quad (10)$$

Here,  $\mathbf{c}$  is the fourth-order spatial elasticity tensor [15] and  $\nabla^s[\cdot]$  is the symmetric gradient operator:

$$\nabla^s[\cdot] = \frac{1}{2} \left[ \frac{\partial[\cdot]}{\partial \boldsymbol{\varphi}} + \left( \frac{\partial[\cdot]}{\partial \boldsymbol{\varphi}} \right)^T \right]. \quad (11)$$

The first two terms in the second line of Eq. (10) are *geometric* and *material stiffnesses*, respectively, from computational mechanics [17]. The image stiffness (second-order tensor) is

$$\mathbf{k} := \frac{\partial^2 U}{\partial \boldsymbol{\varphi} \partial \boldsymbol{\varphi}} = \lambda \left[ \left( \frac{\partial S}{\partial \boldsymbol{\varphi}} \right) \otimes \left( \frac{\partial S}{\partial \boldsymbol{\varphi}} \right) - (T-S) \left( \frac{\partial^2 S}{\partial \boldsymbol{\varphi} \partial \boldsymbol{\varphi}} \right) \right], \quad (12)$$

where “ $\otimes$ ” represents the vector outer product operation.

**2.4 Finite Element Discretization.** A finite element (FE) mesh is constructed to correspond to all or part of the template image.  $T$  is interpolated to the nodes of the FE mesh. As the mesh deforms,  $S$  is queried at the current location of nodes in the template FE mesh. An isoparametric conforming FE approximation is introduced for  $\boldsymbol{\eta}$  and  $\Delta \mathbf{u}$  in Eq. (10):

$$\boldsymbol{\eta}_e := \boldsymbol{\eta}|_{\Omega_e} = \sum_{j=1}^{N_{\text{nodes}}} N_j(\boldsymbol{\xi}) \boldsymbol{\eta}_j, \quad \Delta \mathbf{u}_e := \Delta \mathbf{u}|_{\Omega_e} = \sum_{j=1}^{N_{\text{nodes}}} N_j(\boldsymbol{\xi}) \Delta \mathbf{u}_j, \quad (13)$$

where the subscript  $e$  specifies that variations are restricted to an element with domain  $\Omega_e$ , and  $N_{\text{nodes}}$  is the number of element nodes. Eight-node hexahedral elements with three translational degrees of freedom per node were used, so  $\boldsymbol{\xi} \in \{(-1, 1) \times (-1, 1) \times (-1, 1)\}$  is the bi-unit cube, and  $N_j$  are the isoparametric shape functions. The gradients of  $\boldsymbol{\eta}$  are discretized as

$$\nabla_s \boldsymbol{\eta} = \sum_{j=1}^{N_{\text{nodes}}} \mathbf{B}_j^L \boldsymbol{\eta}_j, \quad \nabla \boldsymbol{\eta} = \sum_{j=1}^{N_{\text{nodes}}} \mathbf{B}_j^{NL} \boldsymbol{\eta}_j, \quad (14)$$

where  $\mathbf{B}^L$  and  $\mathbf{B}^{NL}$  are the linear and nonlinear strain-displacement matrices in Voigt notation [18]. For an assembled FE mesh, Eq. (10) becomes (in Voigt notation):

$$\sum_{i=1}^{N_{\text{nodes}}} \sum_{j=1}^{N_{\text{nodes}}} [\mathbf{K}^R(\boldsymbol{\varphi}^*) + \mathbf{K}^I(\boldsymbol{\varphi}^*)]_{ij} \cdot \Delta \mathbf{u}_j = \sum_{i=1}^{N_{\text{nodes}}} [\mathbf{F}^{\text{ext}}(\boldsymbol{\varphi}^*) - \mathbf{F}^{\text{int}}(\boldsymbol{\varphi}^*)]_i. \quad (15)$$

Equation (15) is a system of linear equations. The term in parentheses on the left-hand side is the (symmetric) tangent stiffness matrix.  $\Delta \mathbf{u}$  is the vector of unknown incremental nodal displacements with length  $[8 \times 3 \times N_{el}]$ , where  $N_{el}$  is the number of elements.  $\mathbf{F}^{\text{ext}}$  is the external force vector arising from Eq. (7), and  $\mathbf{F}^{\text{int}}$  is the internal force vector from the stress divergence. The regularization stiffness arising from the hyperelastic energy is

$$\mathbf{K}^R = \int_{\beta} (\mathbf{B}^{NL})^T \boldsymbol{\sigma} \mathbf{B}^{NL} dv + \int_{\beta} (\mathbf{B}^L)^T \mathbf{c} \mathbf{B}^L dv. \quad (16)$$

The image-based stiffness is

An initial estimate of  $\Delta \mathbf{u}$  is obtained by inverting Eq. (15), and this solution is improved iteratively using a quasi-Newton method [19].

**2.5 Solution Procedure and Augmented Lagrangian.** In Eq. (6), the image data may be treated as either a soft constraint, with the mechanics providing the “truth,” or as a hard constraint, with the mechanics providing regularization, or as a combination. Indeed, Eq. (5) is essentially a penalty function stating that the template and target image intensity fields must be equal as  $\lambda \rightarrow \infty$ . However, as  $\lambda$  is increased,  $\mathbf{K}_I$  becomes ill conditioned, resulting in inaccurate estimates for  $\mathbf{K}_I^{-1}$ , which leads to slowed convergence or divergence of the nonlinear iterations. To circumvent this problem, the augmented Lagrangian method was used [20]. A solution at a particular timestep is first obtained with a relatively small penalty  $\lambda$ . The image-based body forces  $\partial U / \partial \boldsymbol{\varphi}$  are incrementally increased in a second iterative loop, resulting in progressive satisfaction of the constraint. This algorithm allows the constraint to be satisfied to a user-defined tolerance and avoids ill conditioning. Equation (8) is modified by addition of an image-based force  $\gamma$  due to the augmentation:

$$G^* = G(\varphi, \boldsymbol{\eta}) + \int_{\beta} \boldsymbol{\gamma} \cdot \boldsymbol{\eta} \frac{dv}{J} = 0. \quad (18)$$

The augmented Lagrangian update procedure for timestep  $n+1$  takes the form

$\boldsymbol{\gamma}_{n+1}^0 = \boldsymbol{\gamma}_n,$ $k = 0,$ DO for each augmentation $k$ WHILE $\ (\boldsymbol{\gamma}_{n+1}^{k+1} - \boldsymbol{\gamma}_{n+1}^k) / \boldsymbol{\gamma}_{n+1}^k\  > \text{TOL}$ Minimize $G^*$ with $\boldsymbol{\gamma}_{n+1}^k$ fixed using the BFGS method Update multipliers using $\boldsymbol{\gamma}_{n+1}^{k+1} = \boldsymbol{\gamma}_{n+1}^k + (\partial U / \partial \boldsymbol{\varphi})_{n+1}^k$ END DO
---

(19)

Here,  $\boldsymbol{\gamma}_{n+1}^0$  is the starting value for the multiplier vector at time  $n+1$  before the beginning of augmentations,  $k$  is the augmentation number and TOL is the tolerance for defining convergence of the augmentations. This nested iteration procedure (Uzawa algorithm [20]) converges quickly because the multipliers  $\boldsymbol{\gamma}$  are fixed during minimization of  $G^*$ . For the present study, augmentations were performed after  $\lambda$  was increased to the maximum value that could be used without numerical ill conditioning. After this, the augmented Lagrangian method was used with TOL=0.20.

**2.6 Cardiac Image Acquisition.** To mimic typical clinical MR acquisition for patients with cardiac pathologies, gated cine-MRI images of a normal male volunteer’s heart (35 years old) were acquired on a 1.5-T Siemens scanner using standard clinical settings (256 × 256 image matrix, 378 mm FOV, 10-mm slice thickness, ten slices) (Fig. 1). The MRI dataset corresponding to beginning of diastole was designated as the template image. The template image was cropped to a 64 × 64 image matrix by eight slices to focus on the heart.

**2.7 FE Mesh Generation and Boundary Conditions.** The boundaries of the LV were obtained by manual segmentation of the epi- and endocardium from the template image. The 3D FE model was constructed to include the entire image domain, with the lumen and the tissue surrounding the myocardium represented as an isotropic hyperelastic material with relatively soft properties (modulus of elasticity  $E=0.3$  KPa and Poisson’s ratio  $\nu=0.3$ ) so that the entire template image could be mapped. The edges of the mesh were fixed, eliminating rigid motion (see Fig. 2).

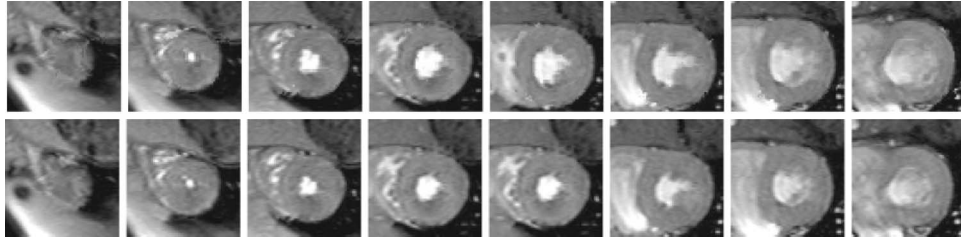


**Fig. 1 Target (top) and template (bottom) image datasets used in the warping analysis. The Target image dataset was created by mapping the template image dataset with displacements determined from a forward FE simulation of passive diastolic filling.**

**2.8 Constitutive Model and Material Coefficients.** The myocardium was represented as transversely isotropic hyperelastic with fiber angle varying from  $-90$  deg at the epicardial surface to  $90$  deg at the endocardial surface [21]. The model represented fibers in a neo-Hookean matrix:

$$W = \mu(\tilde{I}_1 - 3) + F_2(\tilde{\lambda}) + \frac{K}{2}[\ln(J)]^2. \quad (20)$$

$\tilde{I}_1$  is the first deviatoric invariant of  $\mathbf{C}$  [22],  $\tilde{\lambda} = \sqrt{\mathbf{a}_0 \cdot \tilde{\mathbf{C}} \cdot \mathbf{a}_0}$  is the deviatoric fiber stretch along the local direction  $\mathbf{a}_0$ ,  $\mu$  is the shear modulus of the matrix, and  $K$  is the bulk modulus. The fiber stress-stretch behavior was represented as exponential, with no resistance to compressive load:

$$\tilde{\lambda} \frac{\partial F_2}{\partial \tilde{\lambda}} = 0, \quad \tilde{\lambda} < 1,$$

$$\tilde{\lambda} \frac{\partial F_2}{\partial \tilde{\lambda}} = C_3[\exp(C_4(\tilde{\lambda} - 1)) - 1], \quad \tilde{\lambda} \geq 1. \quad (21)$$

Here,  $C_3$  scales the stresses and  $C_4$  defines the fiber uncrimping rate. A description of the constitutive model and its FE implementation can be found in Weiss et al. [23].

Material coefficients were determined by a nonlinear least-squares fit of the constitutive equation to published equibiaxial stress/strain curves [24] ( $\mu=2.10$  KPa,  $C_3=0.14$  KPa, and  $C_4=22.0$ ). A bulk modulus  $K$  of 160.00 KPa was chosen so that changes in relative volume were under 5%, in other words the material would be nearly incompressible. The LV material properties do not need to be exact for this analysis because stretch and strains from the forward FE model were used as the “gold standard” for comparison to warping results. A physiological internal pressure was applied to the endocardial surface and a nonlinear

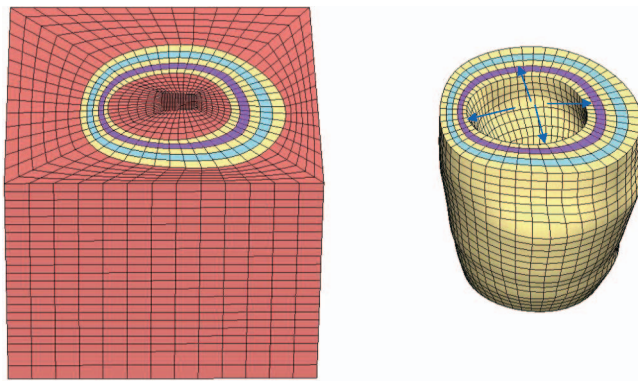


**Fig. 2 (Color) Left: Forward FE model used to create target image. Right: Detail of the LV. Blue arrows indicate that external pressure was applied on the endocardial surface.**

FE analysis was performed using NIKE3D [25]. Predictions of fiber stretch, circumferential, radial and in-plane (radial-circumferential) shear strains were compared to values in the literature.

**2.9 Creation of Synthetic Target Image.** To validate warping predictions of strain, a pair of 3D MRI image datasets representing two deformation states of the LV were used such that the deformation map between the states represented in the images was known. A synthetic target image was created by applying the displacement map of the forward FE model to the template MRI image (Fig. 1). These image datasets were used as the only input in the warping analysis; pressure boundary conditions were not applied.

**2.10 Comparison of Synthetic End-diastolic Image With In Vivo End-diastolic image data set.** The simulated end-diastolic image data set (Target) and the in vivo end-diastolic image data set were compared to determine the similarity of the images using two standard image similarity measures that are independent of the image energy functional: the Hausdorff distance [26] and the Chamfer distance [27]. These measures were also determined for the template image data set and the in vivo image data set for comparison purposes. The Chamfer distance is the average distance (in pixels) for every edge point in one image to the nearest edge in the other. The Hausdorff distance [26] gives the maximum distance over all of the edge points in one image to the nearest edge in the other (it gives the distance for that edge which is farthest to the nearest edge in the other image). The Hausdorff distance gives the “worst case” of mismatch between two images. It should be noted that the forward model, which the synthetic image data set was based upon, was not designed to reproduce the deformation documented in the in vivo image data set. Rather, it was designed to have deformation values during diastole that were consistent with those reported in the literature.

**2.11 Warping Model.** The warping FE model used the same geometry and material properties as the forward FE model. The tether mesh was not included because it was only necessary to determine deformation measures within the LV wall. Nodal values of fiber stretch, circumferential, radial, and shear strain were averaged for each image slice and compared with values from the forward FE model. To assess transmural deformation, the same measures were computed as a function of wall position. Scatter plots were generated to determine coefficients of determination ( $R^2$ ) between warping and forward FE model predictions. A Bland-Altman analysis [28] was performed to assess agreement between the forward FE and warping predictions for the four measures of deformation. Absolute and percent rms errors were calculated using

$$\text{rms error} = \sqrt{\frac{1}{N_{\text{nodes}}} \sum_{i=1}^{N_{\text{nodes}}} (\epsilon_{\text{forward}} - \epsilon_{\text{warp}})^2}, \quad (22)$$

and

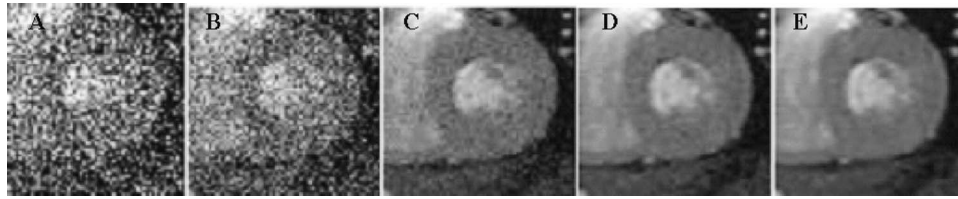


**Fig. 3 Effect of increasing levels of additive noise on the appearance of one slice from the template image dataset. (A) SNR=0.5, (B) SNR=1, (C) SNR=4, (D) SNR=8, and (E) SNR=16.**

$$\text{percent rms error} = \sqrt{\sum_{i=1}^{N_{\text{nodes}}} \frac{(\epsilon_{\text{forward}} - \epsilon_{\text{warp}})^2}{(\epsilon_{\text{forward}})^2}}. \quad (23)$$

Here,  $\epsilon_{\text{forward}}$  represents a forward analysis strain value for a given node,  $\epsilon_{\text{warp}}$  is the predicted strain value for the corresponding node in the warping analysis and  $N_{\text{nodes}}$  is the total number of nodes in the elements representing the myocardial wall. For fiber stretch, percent rms error was calculated by first subtracting a value of 1.0 from the data to convert stretch to units of strain.

**2.12 Edge versus Wall Warping Solution.** Since the warping body force is based on image intensity and gradient [Eq. (7)], it was expected that predictions would be more accurate for the endo- and epicardial boundaries in comparison to mid-wall.  $R^2$  values were calculated between the strain/stretch warping and FE predictions for nodes on the endo- and epicardial surfaces. These  $R^2$  values were compared with values for the entire model on each image plane.

**2.13 Sensitivity to Material Coefficients and Constitutive Model.** To determine the sensitivity of warping to changes in material coefficients,  $\mu$  and  $C_3$  were increased and decreased by 24% of the baseline values, corresponding to the 95% confidence interval of the data in Humphrey et al. [29]. To assess the importance of the fiber reinforcement, the constitutive model was changed to an isotropic neo-Hookean model for the warping simulations. Finally, the effect of the material bulk modulus was assessed by increasing and decreasing  $K$  by a factor of 10.0 in the warping analysis. To measure the effect of the changes in material properties and the change in material model, the  $R^2$  values, rms errors and the percent rms errors were determined for the four measures of local strain between the warping and forward FE model predictions.

**2.14 Sensitivity to Image Noise.** To assess the effects of noise on the warping predictions, an additive noise model was used to modify the images [30]. Random noise  $N(i, j)$  was added to the images  $I(i, j)$ , where  $i$  and  $j$  represent pixel coordinates, to create a noisy image  $S(i, j)$ :

$$S(i, j) = I(i, j) + N(i, j). \quad (24)$$

The noise intensities  $N(i, j)$  were defined as a zero mean probability distribution with the standard deviation  $\sigma_N$  [30]. The signal-to-noise ratio (SNR) was defined as

$$\text{SNR} = \frac{\sigma_I}{\sigma_N}. \quad (25)$$

For the images used,  $\sigma_I = 42$  gray levels. SNRs of 16, 8, 4, 1, and 0.5 were examined (Fig. 3). The measures of deformation obtained from Warping using the noisy images were compared with predictions from the forward FE model to determine the effect of SNR on the  $R^2$  values and the associated rms errors.

**2.15 Sensitivity to the Addition of Intermediate Diastolic Image Data.** To assess the effects of the use of intermediate image data on the end-diastolic warping predictions, additional image data sets representing intermediate stages of diastolic filling were created in the manner detailed using the forward FE model. Three intermediate target image data sets were used, representing the first quarter of filling, mid-diastole and late diastole. Warping analyses were performed using all of the immediate images, using only two intermediate image sets (mid-diastole and late diastole), and using only a mid-point diastolic image added to determine the contribution of the additional data to the overall accuracy of the end-diastolic solution.

**2.16 Accuracy of Strain Predictions of Intermediate Diastolic Image Data.** Warping analyses were performed with each of the intermediate target images discussed in the previous section to determine accuracy of the intermediate solutions. The warping strain predictions were compared with forward FE solution for the intermediate filling stages. The rms errors and the relative rms errors were determined for each of these analyses and compared with the baseline validation study.

### 3 Results

**3.1 Forward FE Model Predictions.** Forward FE predictions of myocardial strains during diastole were in good agreement with values in the literature (Table 1), demonstrating that the images

**Table 1 Comparison of forward FE strain predictions for changes in strain between beginning and end diastole to values reported in the literature. The forward FE results are in reasonable agreement with published experimental results.**

Strain Component	Forward FE Model		Sinusas [7]		Guccione [64]		Omens [44]	
	Epi	Endo	Epi	Endo	Epi	Endo	Epi	Endo
Circumferential	0.22	0.07	0.15	0.07	0.15	0.09	0.22	0.05
Radial	0.14	0.09	0.25	0.15	0.34	0.19	0.18	0.12
In-plane Shear	0.08	0.03	>0.02		0.06	0.01	0.03	0.02 <sup>a</sup>

<sup>a</sup>Reported a mid-wall peak of 0.08.

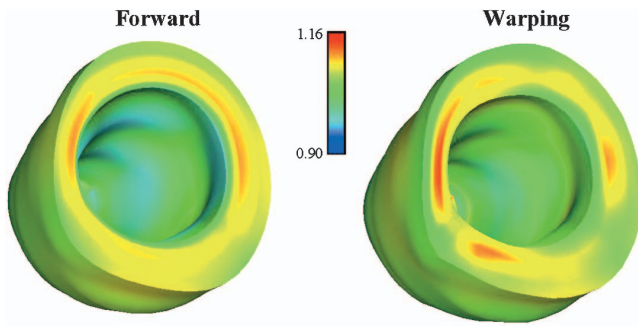


**Fig. 4 (Color)** Fiber stretch distribution for the forward FE (left) and warping (right) analyses. The fiber stretch distributions show good agreement between the FE and the warping analyses.

derived using the deformation map from the forward FE model provided a reasonable surrogate for validation of warping predictions. Circumferential strains were in excellent agreement [7,31,32]. Endocardial and epicardial radial strains were comparable to values reported by Omens [31] and somewhat less than those reported by others [7,32]. In-plane shear strains were also

generally consistent with results from Guccione [32] and Omens [31], while Sinusas et al. [7] reported a very low in-plane shear strain. The forward FE model did not predict a clear peak in the shear strain near the mid-wall. Average fiber stretch (Fig. 6(A),  $1.09 \pm 0.01$ ) was slightly lower than that reported by Tseng et al. [33] ( $1.12 \pm 0.01$ ) for the midventricle and by MacGowan et al. [34] (1.15) for the entire LV. Forward FE model prediction of end-diastolic diameter was 46 mm which is consistent with values in the literature [35].

The Chamfer distance between the synthetic target image data set and the in vivo end-diastolic image data was 1.49 mm, while the Hausdorff distance was 5.75 mm. For comparison, the Chamfer distance and Hausdorff distance between the template image data set and the in vivo end-diastolic image data set were 1.77 and 8.90 mm, respectively. Note that these similarity measures cannot be computed between the deformed template and the target or in vivo end-diastolic images since only the ventricular wall was discretized and tracked in the warping analyses.

### 3.2 Comparison of Forward FE and Warping Predictions.

There was good qualitative and quantitative agreement between forward and warping predictions of fiber stretch (Figs. 4 and 5(A)). The highest fiber stretch was 40–50 % through the wall, decreasing toward the endo- and epicardial surfaces. Fiber stretch was slightly higher at the endocardial surface than the epicardial

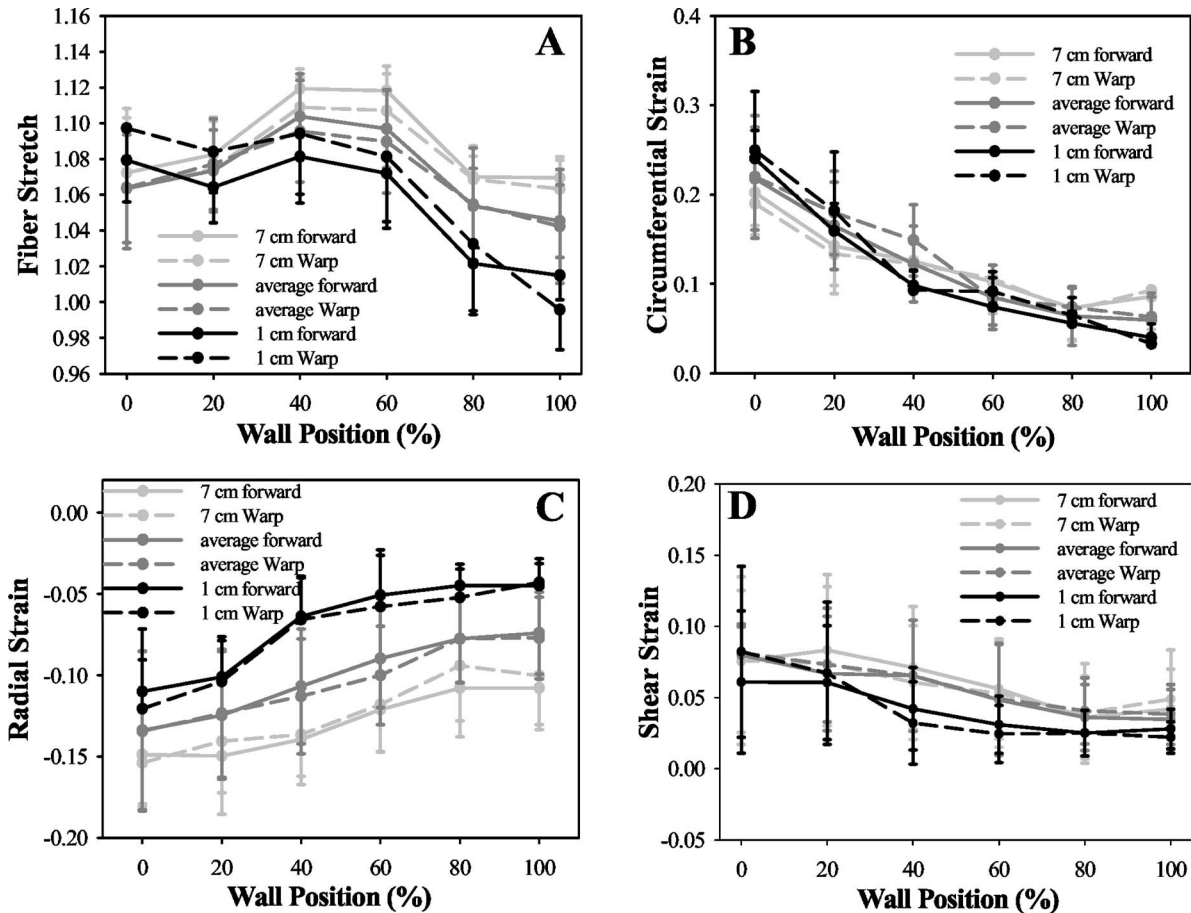


**Fig. 5** Forward and FE predictions of several measures of local wall deformation at end diastole as a function of distance through the myocardial wall (mean  $\pm$  standard deviation). **A:** local fiber stretch. **B:** circumferential Green-Lagrange strain. **C:** radial Green-Lagrange strain. **D:** in-plane Green-Lagrange shear strain (circumferential/radial). 0% denotes endocardial surface and 100% denotes epicardial surface. Results are presented for image cross-sectional slices at 1 cm (light gray), 7 cm (dark gray), and as an average over all slices (black). 7 cm corresponds to the base of the LV and 1 cm is near the apex of the heart. Solid lines indicate results for the forward FE model and dashed lines indicate results for hyperelastic warping. Error bars show standard deviations. All values are referenced to the undeformed geometry (beginning diastole).

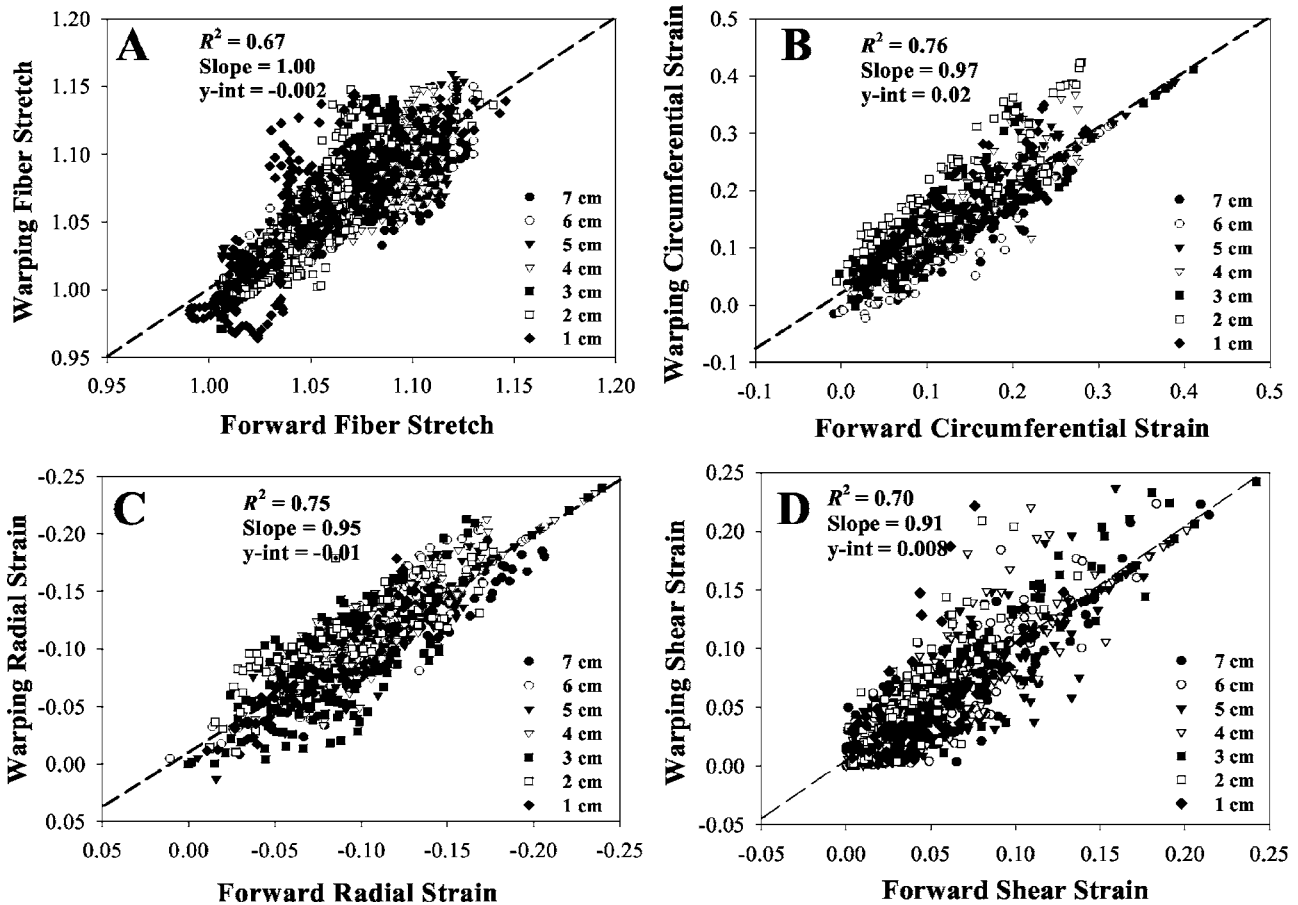


**Fig. 6** Scatter plots of forward FE versus warping stretch/strains. **A:** fiber stretch. **B:** circumferential strain. **C:** radial strain. **D:** in-plane shear strain. Symbols represent different axial image slices. 7 cm corresponds to the base of the LV and 1 cm is near the apex of the heart.

surface. The magnitudes of circumferential, radial and shear strain were highest at the endocardial wall and decreased toward the epicardial surface (Figs. 5(B), 5(C), and 5(D)). There was very good agreement between the forward FE and warping predictions in terms of the magnitudes of strains and their transmural variation for all four measures of local deformation.

Average fiber stretch and strains for the warping and forward FE results had generally higher standard deviations than averages for individual planes (Fig. 5). Thus, variability depicted in the overall average is partially due to variability between image planes. Differences between axial locations are expected because of differences in LV geometry from apex to base.

There was a significant correlation between forward FE and warping predictions for all measures of strain ( $p < 0.001$  for all cases) (Figs. 6(A)–6(D)). Circumferential strain predictions had the highest  $R^2$  value  $R^2 = 0.76$ , while fiber stretch predictions had the lowest  $R^2 = 0.67$ . The Bland-Altman analyses indicated good agreement between the forward FE solution and the warping predictions with the strain measures (Figs. 7(B)–7(D)) showing no apparent bias (all regression slopes  $\leq 0.099$ ). The stretch results (Fig. 7(A)) indicated a slight tendency for the warping analysis to under-predict the stretch at low stretch values and over-predict the stretch at high stretch values (regression line slope = 0.22).

**3.3 Edge versus Wall Warping Solution.** Predictions based on nodes on the epi- and endocardial surfaces had slightly better correlation with forward FE results than those based on all nodes in the model (Table 2).  $R^2$  values for in-plane strains (circumferential, radial, shear) were consistently higher than for fiber stretch.

**3.4 Sensitivity to Changes in Material Coefficients and Constitutive Model.** Warping predictions of fiber stretch and strain were insensitive to changes in the material parameters  $\mu$  and  $C_3$  (Table 3). When the constitutive model used in the warping analysis was changed from transversely isotropic to neo-Hookean, predictions for all four measures of strain were affected.  $R^2$  values dropped from one to ten points. The increases in percent rms error ranged from 1% (shear strain) to 10% (fiber stretch) and the increases in absolute rms error ranged from 0.000 (shear strain) to 0.005 (fiber stretch) (Table 3). Predictions were also sensitive to changes in the bulk modulus ( $K$ ), depending on whether the material was made more or less compressible. Increasing  $K$  by an order of magnitude resulted in a decrease in  $R^2$  for in-plane strains and increases in both rms error and percent rms error. Decreasing  $K$  by an order of magnitude resulted in severe degradation of the  $R^2$  values and resulted in substantial increases in rms error and percent rms error for all measures of deformation.

**3.5 Sensitivity to Image Noise.** There was little change in the  $R^2$  values or rms error between forward FE and warping predictions down to a SNR of 4.0. Decreases in the  $R^2$  values and increases in rms error was progressive for SNRs below 4.0 (Fig. 8).

**3.6 Addition of Intermediate Diastolic Image Data.** The addition of intermediate image data slightly improved the accuracy of the analyses. The overall change in rms error for all measures of strain were less than 0.03 with an associated improve-

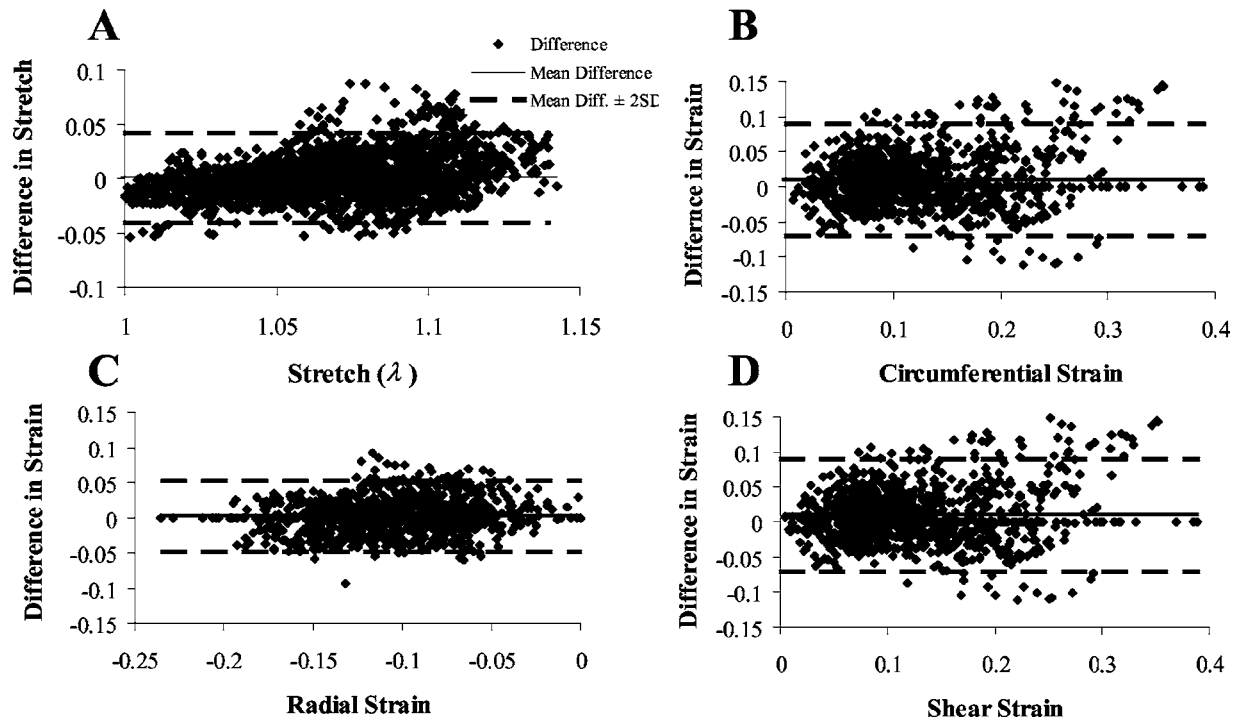


**Fig. 7 Bland-Altman plots of the validation stretch and strain comparison. A: fiber stretch. B: circumferential strain. C: radial strain. D: in-plane shear strain. The plots show good agreement between the forward and warping solutions. The central solid line indicates the mean difference in the data while the heavy dashed lines indicate the boundary of  $\pm 2$  standard deviations.**

ment in relative rms error of less than 4%. The initial addition of a single mid-diastolic image produced the slight increase in accuracy. The addition of the early diastolic image data and a late diastolic image data set did not produce any further improvement in the accuracy of the predictions regardless of whether the augmented Lagrangian analyses were performed at the intermediate image sets.

**3.7 Accuracy of Strain Predictions of Intermediate Diastolic Image Data.** The warping analyses on each of the intermediate image data sets showed that the accuracy of the intermediate solutions themselves were comparable to the full diastolic validation solution (Table 4) with similar values for rms errors. The relative rms errors showed increasing values at the late diastolic and mid-diastole analyses with the highest relative rms errors being found in the early diastolic analysis due to the decreasing average deformation.

#### 4 Discussion

In the present study, minimization of the image-based energy was enforced in a “hard” sense using an augmented Lagrangian technique, while a hyperelastic strain energy was used to regularize the image registration. These approaches are considered to be major strengths of the method. The use of a hyperelastic strain energy in combination with a FE discretization ensures that deformations will be diffeomorphic (one-to-one, onto, and differentiable with a differentiable inverse; see, e.g., Ref. [36]). Second, hyperelasticity is objective for large strains and rotations, while previous use of solid mechanics-based regularizations were based on linear elasticity [37–40], which is not objective and penalizes large strains and rotations. Finally, the use of a realistic constitutive model for the LV ensures that deformation maps reflect the behavior of an elastic material under finite deformation. In regions of the template model that have large intensity gradients, large

**Table 2 Coefficients of determination ( $R^2$ ) between forward FE and warping predictions of stretch and strain for each image slice. Correlations are presented using data for the entire models (“Wall”) and using only the boundary nodes (“Boundary”). The  $R^2$  for the boundary nodes were slightly better for the entire model in most cases. The coefficients of determination for in-plane measures of strain (circumferential, radial, shear) had consistently higher  $R^2$  values than for fiber stretch.**

Slice	Fiber Stretch		Cir. Strain		Radial Strain		Shear Strain	
	Wall	Boundary	Wall	Boundary	Wall	Boundary	Wall	Boundary
7	0.66	0.81	0.75	0.87	0.72	0.76	0.72	0.85
6	0.58	0.45	0.85	0.90	0.76	0.79	0.76	0.79
5	0.71	0.74	0.79	0.81	0.71	0.77	0.76	0.83
4	0.62	0.71	0.85	0.85	0.77	0.85	0.77	0.77
3	0.76	0.83	0.77	0.74	0.66	0.74	0.84	0.85
2	0.71	0.71	0.79	0.79	0.67	0.66	0.67	0.72
1	0.72	0.76	0.88	0.88	0.71	0.88	0.71	0.76
Avg	0.68 $\pm$ 0.06	0.72 $\pm$ 0.13	0.81 $\pm$ 0.06	0.83 $\pm$ 0.06	0.71 $\pm$ 0.04	0.78 $\pm$ 0.07	0.75 $\pm$ 0.05	0.80 $\pm$ 0.05

**Table 3** Effect of changes in material coefficients and constitutive model on coefficients of determination ( $R^2$ ), rms error (units of strain), and the percent rms error between the warping and forward FE predictions for the four measures of strain. “ $\mu+24\%$ ” indicates that results are for the 24% increase in  $\mu$ , the shear modulus.

	Fiber Strain			Circ. Strain			Radial Strain			Shear Strain		
	$R^2$	rms error	% rms error	$R^2$	rms error	% rms error	$R^2$	rms error	% rms error	$R^2$	rms error	% rms error
Baseline Warping	0.67	0.021	29	0.72	0.041	30	0.66	0.025	22	0.70	0.026	36
$\mu+24\%$	0.65	0.021	30	0.69	0.044	32	0.65	0.025	23	0.71	0.026	36
$\mu-24\%$	0.64	0.021	29	0.70	0.042	30	0.65	0.025	23	0.70	0.026	36
$C_3+24\%$	0.65	0.021	30	0.71	0.040	29	0.66	0.026	23	0.72	0.024	34
$C_3-24\%$	0.65	0.021	30	0.70	0.041	30	0.66	0.026	23	0.72	0.024	34
Neo-Hookean	0.57	0.026	39	0.65	0.049	35	0.58	0.032	28	0.69	0.026	37
$K \times 10$	0.55	0.021	32	0.63	0.047	42	0.65	0.035	31	0.63	0.028	39
$K/10$	0.50	0.042	58	0.40	0.079	57	0.30	0.060	53	0.27	0.050	70

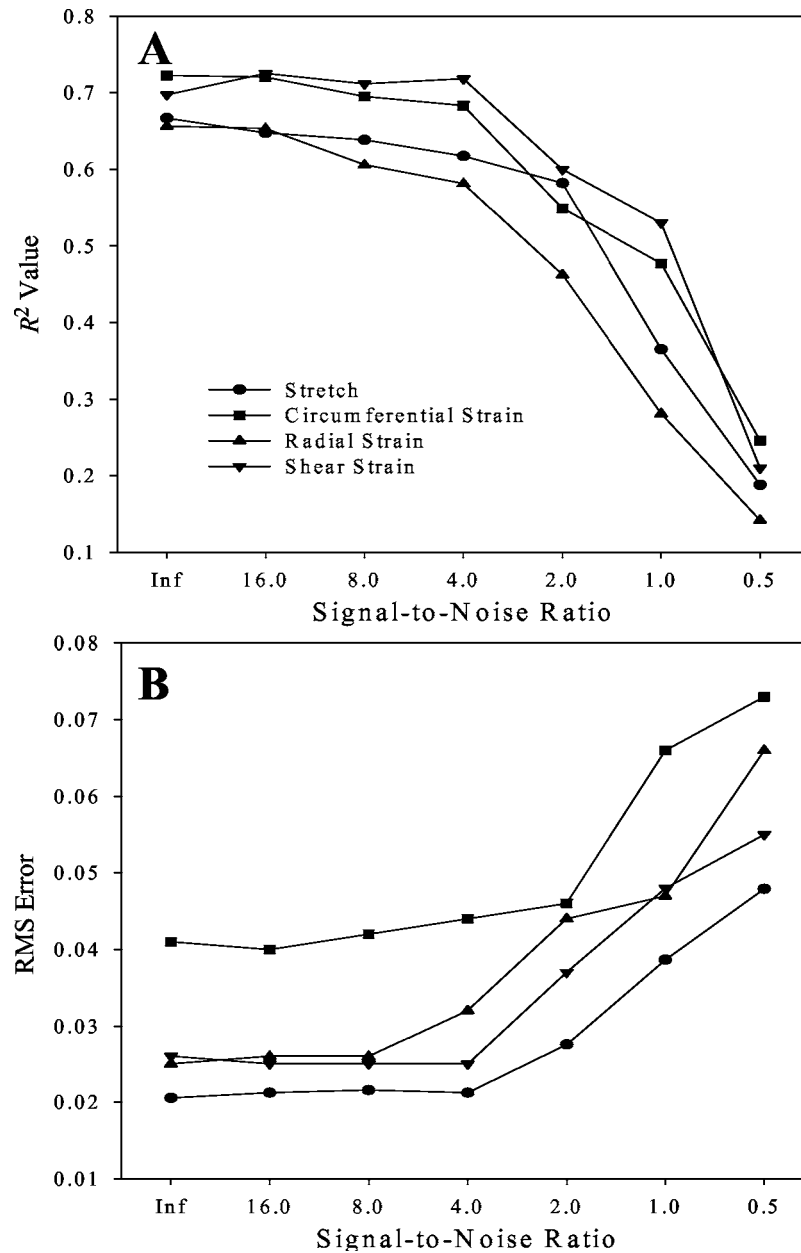


**Fig. 8** Effect of signal-to-noise ratio on **A**: coefficient of determination; and **B**: the RMS error (units of strain) for the four measures of deformation

**Table 4 The accuracy of the analyses of the intermediate image data sets show similar error magnitudes for rms error as found in the original validation study. The percent rms error was found lowest for the end-diastolic study, with the percent rms error increasing with decreasing average deformation. The percent rms was the highest in the early diastolic analysis where the rms error was found to be nearly the magnitude of the measured strain and in the case of the shear measurement the rms error was larger than the measured shear strain.**

Target Image Data Set	Fiber Strain		Circ. Strain		Radial Strain		Shear Strain	
	rms error	% rms error	rms error	% rms error	rms error	% rms error	rms error	% rms error
Early diastolic image	0.017	60	0.034	62	0.025	87	0.023	120
Mid-diastolic image	0.016	45	0.028	45	0.024	39	0.020	34
Late diastolic image	0.018	34	0.036	54	0.025	35	0.021	31
End-diastolic image	0.021	29	0.041	30	0.025	22	0.026	36

image-based forces will be generated and the solution will be primarily determined by the image data. In regions that lack image texture or gradients, image-based forces will be smaller and the predicted deformation will be more dependent on the hyperelastic regularization (material model). A realistic representation of the material behavior helps to improve predictions in these areas. Other techniques for image-based strain measurement, such as optical flow [41] and texture correlation [42], use only an image-based energy term. These techniques do not ensure physically reasonable deformations in regions that lack image contrast or texture and they are sensitive to noise [42]. Further, there is no guarantee that deformation maps will be diffeomorphic.

The points above can be examined in the context of comparisons between the forward FE and warping predictions. Generally,  $R^2$  values for fiber stretch and strains were slightly better on the epicardial and endocardial surfaces than for the overall model (Table 2). This is consistent with the notion that regions with high gradients in image intensity yield better results. However, it is notable that predictions for the entire model (including locations within the myocardial wall) were not much worse. The loss of accuracy for the mid-wall predictions do not drop to unacceptable levels, particularly for the in-plane strain measurements. In fact, overall predictions from hyperelastic warping correlated very well with forward FE predictions (Fig. 6), and warping predicted transmural gradients in strains and fiber stretch with good fidelity (Fig. 5). The worst correlation between forward FE and warping was obtained for fiber stretch ( $R^2=0.67$ , Fig. 6(A)). The image data used in this study had a 1-cm slice thickness, which was likely the main factor that resulted in the lower correlations for fiber stretch.

Despite reasonable agreement with strain measurements in the literature, several shortcomings of the forward FE model are worth noting. First, orthotropic material symmetry may provide a more accurate representation of the passive material properties of myocardium than transverse isotropy, since it can represent the laminar (sheet) organization of ventricular myofibers and thus accommodate differences in transverse stiffness [43]. Second, the forward FE model predicted mid-wall fiber stretches that were higher than those at the endo- and epicardial surfaces (Fig. 5(A)), while reported transmural fiber strains during diastole and systole are generally uniform [7,33,44,45]. Most of these studies reported systolic strain measurements with diastole as the reference configuration. Interestingly, in a canine study of diastolic strains [6], a difference of 23% in fiber strain was reported between the inner wall of the myocardium ( $\sim 0.17$ ) and the outer/mid-wall ( $\sim 0.22$ ). Similarly, MacGowan et al. [34] measured a statistically significant difference in systolic fiber shortening between epicardium and endocardium in normal human subjects. These studies suggest that forward FE predictions of transmural fiber strain may be reasonable. Finally, although the FE model geometry was patient-specific, the fiber angle distribution was idealized. Despite these shortcomings, it must be emphasized that the most important aspects of the forward FE model were that it provided a reasonable approximation of passive ventricular mechanics, the exact

solution for the strains was known, and a synthetic image dataset corresponding to that exact solution could be generated. A similar approach to validation, based on forward FE predictions, has been used previously to validate measurements of ventricular strain based on spline interpolation of MRI tissue tags [46].

Warping predictions of fiber stretch and strain were relatively insensitive to changes in material properties with the exception of the bulk modulus. An order of magnitude increase in the bulk modulus ( $K$ ) of the material had little effect on the in plane strain predictions, however, the fiber stretch predictions showed degradation. Decreasing  $K$  by an order of magnitude led to unacceptable degradation of the predicted values and a substantial increase in rms error. This indicates that a reasonable estimation of the myocardium bulk modulus is necessary for accurate predictions. The forward FE model, baseline warping model and the model with increased bulk modulus showed less than 5% change in relative volume, while the warping model with decreased bulk modulus resulted in volume changes up to 21% indicating that the material bulk response had become quite compressible.

The use of an isotropic material model instead of a transversely isotropic material model in the warping simulations resulted in decreased  $R^2$  values with increased rms errors. This was likely due to the importance of the material model in regions of the template that have little image texture or gradients. As mentioned earlier, these regions generate little image force to deform the template model. Even with the appropriate material model and exact material property definitions, areas with a high intensity gradient (epi- and endocardial surfaces) provide slightly better predictions (average increase in  $R^2=0.035$ ) than those based on the entire wall (Table 2). Whereas cine-MRI images provide some inhomogeneities within the myocardial wall (Fig. 1), warping predictions based on imaging modalities such as CT, where the myocardial wall intensity is homogeneous, would depend on the geometry, the accuracy of the material model and parameters assigned to the warping model. Future investigations should examine the ability of warping to predict strains in the myocardium with the presence of simulated ischemic or infarcted regions.

Warping was relatively insensitive to image noise. The warping analyses did not show a decrease in the predicted  $R^2$  values nor an increase in rms error down to SNR values of 4.0. This suggests that the technique may be applicable to relatively noisy image modalities such as positron emission tomography (PET) or single photon emission computed tomography (SPECT) [47]. Previous work has suggested that the deformation distributions determined by warping on a PET image data set produces comparable results as those determined from cine-MRI image data sets of the same patient [48]. However, further study and validation is necessary before warping can be used with PET image datasets.

Techniques that have been used to evaluate LV mechanical function can broadly be categorized into those that determine global measures of LV deformation and those that determine local measures of LV deformation. LV wall function is typically evaluated using 2D Doppler echocardiography by interrogating the LV

from various views to obtain an estimate of 3D segmental wall motion or wall thickening [2]. Additionally, 1D *M*-mode Doppler has been used to give estimates of myocardial thickening and strain. These echocardiographic measurements can be subjective and experience dependent [49] and are not three dimensional. Three-dimensional echocardiography can provide full 3D views of the LV, but can be limited to certain acquisition windows that may lead to obstructed views of the LV. In a similar fashion to echocardiography, cine-MRI has been used for wall motion and wall thickening analyses [3]. While not as convenient as echocardiography in the clinical setting, cine-MRI is fully three dimensional and does not depend on specific interrogation windows to visualize the LV. Radionuclide ventriculography is the most widely used technique for assessment of left ventricular ejection fraction (LVEF) in heart failure [50]. In conjunction with global LVEF and assessment of diastolic function, regional wall motion analysis has been used to study the effect of drugs on the underlying pathophysiological process [4].

Although wall motion and wall thickening are useful measures of wall function, the measurement of local strain or fiber contraction or extension (stretch) provides three-dimensional information on mechanical function of the myocardium. The most widely used technique for quantifying local myocardial strain is MR tagging [51–53]. MR tagging relies on local perturbation of the magnetization of the myocardium with selective radio-frequency (rf) saturation to produce multiple, thin tag planes. The resulting magnetization lines, which persist for up to 400 ms, can be used to track the deformation of the myocardium. The tags provide fiducials for the calculation of strain. The primary strength of tagging is that in vivo, noninvasive strain measurements are possible [54,55]. It can effectively track fast, repeated motions in three dimensions. Further, to determine 3D deformation, two to three orthogonal tag sets must be acquired at all time instances [56]. The resolution of the deformation map determined from tagging is dependent on the tag spacing rather than the resolution of the MRI acquisition matrix, with an optimal tag spacing of six pixels [57]. Hyperelastic warping offers the flexibility of being able to be used on more than a single imaging modality. The spatial resolution of hyperelastic warping depends on the sampling of the template and target images via the FE mesh discretization, which can be refined to equal or surpass the resolution of the MR acquisition matrix. Depending on the textural quality of the image data, analyses using higher-resolution spatial discretizations may or may not result in improved accuracy for strain predictions.

Although an idealized fiber angle distribution was used in the validation analyses, more accurate average or subject-specific fiber angles could be incorporated. Combining tagged deformation data with a separate finite element model incorporating fiber structure has been demonstrated by Tseng et al. [33]. While diffusion tensor MRI (DTMRI) has the potential to provide patient-specific fiber distribution information, difficulties with long acquisition times and motion artifacts make in vivo acquisition extremely difficult [58,59]. In cases where the fiber distribution cannot be estimated, for example, where extensive remodeling due to pathologies such as cardiomyopathy and myocardial infarction have taken place, fiber stretch estimates based on population averages would likely not be reliable. Nevertheless, the sensitivity studies (Table 3) suggest that reasonable predictions of diastolic strains may still be possible in the absence of accurate data on the spatial distribution of fiber angles.

Several additional improvements in hyperelastic warping and other applications of the technique are envisioned. Warping has the potential to be able to estimate the left ventricular wall *stress* during diastolic filling. To estimate stress, accurate boundary conditions and constitutive relations are critical. Estimates of intraventricular and intrathoracic pressure would need to be added to the warping analysis. The effects of residual stress would need to be included, since even in the absence of contraction or intraventricular pressure, the myocardium is not stress free [60,61]. Addi-

tionally, hyperelastic warping could be used to estimate material coefficients for a constitutive model. Using both the image forces determined by the warping analysis and measurements or estimates of the physiological loading (e.g., intraventricular pressure, intrathoracic pressure), the material property coefficients used to characterize the passive myocardium could be estimated via a nonlinear optimization technique [62]. This method would determine the configuration where the physiological loading and the material behavior of the model would best reproduce the deformation documented in the images. The accuracy of strain predictions from hyperelastic warping could be improved by using a priori information regarding the location of distinct anatomical landmarks, such as the junctions between the left and right ventricles. Since the technique is based on a FE discretization, imposition of such displacement boundary conditions is straightforward.

The use of a time series of target images allowed for temporal tracking of diastolic deformation with consistent accuracy throughout the filling phase. It appears that two images provide reasonable accuracy to determine diastolic deformation since the use of multiple target images did not result in improvement in the accuracy of diastolic deformation. However, multiple target images would likely be necessary estimate strain during systole. Multiple targets would allow the warping model would follow a more realistic deformation path than that taken during the analysis using two image data sets. However, preliminary tests for the use of warping to determine systolic deformation indicates that the warping analysis of systolic deformation may be prone to element inversion during the nonlinear iteration process, leading to a failure of the analysis. This is not surprising given that systolic deformations involve generally larger deformations. Further research is necessary to determine whether the warping technique can be applied to strain measurement during systole, and it is expected that it may be difficult to determine some components of systolic strain such as transverse shear. Comparisons with other techniques such as MR tagging would be useful to validate warping predictions during systole.

It should be possible to use tagged MR images and standard cine MR images with hyperelastic warping simultaneously. By including additional energy terms that forced registration of the tag lines in a separate tagged dataset [63], warping would provide additional information to drive the registration based on the image data that could potentially improve spatial resolution and accuracy that could be obtained by either technique if used alone. In theory this approach could be applied to image data obtained via other modalities as well, combining for instance one image functional based on MR images and another based on CT images.

In summary, the results of this study indicate that hyperelastic warping can predict simulated strain and fiber stretch distributions of the left ventricle during diastole from the analysis of cine-MRI images acquired with scanner settings and image resolution that are typical of those used clinically. Warping predictions of in-plane strains showed better agreement with predictions from the forward FE model than the fiber stretch predictions. Warping predictions were most accurate in regions of high intensity gradients such as the endo- or epicardial surfaces. The material parameter–model sensitivity studies demonstrated that strain predictions are not highly dependent on the material coefficients used to regularize the registration problem, with the exception that a reasonable estimate of the bulk modulus of the material is needed. Warping can accurately determine fiber stretch distribution in relatively noisy images, down to a SNR of 4.

## Acknowledgments

Financial support from NIH Grant No. R01-EB00121, NSF Grant No. BES-0134503, and by the U.S. Department of Energy under Contract No. DE-AC03-76SF00098, is gratefully acknowledged. An allocation of computer time was provided by the Center for High Performance Computing at the University of Utah. The

authors thank Gregory J. Klein for providing image data.

## References

- [1] D'Hooge, J., Konofagou, E., Jamal, F., Heimdal, A., Barrios, L., Bijnens, B., Thoen, J., Van de Werf, F., Sutherland, G., and Suetens, P., 2002, "Two-dimensional ultrasonic strain rate measurement of the human heart in vivo," *IEEE Trans. Ultrason. Ferroelectr. Freq. Control*, **49**, pp. 281–286.
- [2] Weidemann, F., Kowalski, M., D'Hooge, J., Bijnens, B., and Sutherland, G. R., 2001, "Doppler myocardial imaging. A new tool to assess regional inhomogeneity in cardiac function," *Basic Res. Cardiol.*, **96**, pp. 595–605.
- [3] Plein, S., Smith, W. H., Ridgway, J. P., Kassner, A., Beacock, D. J., Bloomer, T. N., and Sivananthan, M. U., 2001, "Qualitative and quantitative analysis of regional left ventricular wall dynamics using real-time magnetic resonance imaging: Comparison with conventional breath-hold gradient echo acquisition in volunteers and patients," *J. Magn. Reson. Imaging*, **14**, pp. 23–30.
- [4] Lahiri, A., Rodrigues, E. A., Carboni, G. P., and Rafferty, E. B., 1990, "Effects of chronic treatment with calcium antagonists on left ventricular diastolic function in stable angina and heart failure," *Circulation*, **81** (suppl III), pp. 130–138.
- [5] McVeigh, E. R., and Zerhouni, E. A., 1991, "Noninvasive measurement of transmural gradients in myocardial strain with MR imaging," *Radiology*, **180**, pp. 677–683.
- [6] Takayama, Y., Costa, K. D., and Covell, J. W., 2002, "Contribution of laminar myofiber architecture to load-dependent changes in mechanics of LV myocardium," *Am. J. Physiol. Heart Circ. Physiol.*, **282**, pp. H1510–H1520.
- [7] Sinusas, A. J., Papademetris, X., Constable, R. T., Dione, D. P., Slade, M. D., Shi, P., and Duncan, J. S., 2001, "Quantification of 3-D regional myocardial deformation: Shape-based analysis of magnetic resonance images," *Am. J. Physiol. Heart Circ. Physiol.*, **281**, pp. H698–H714.
- [8] Guccione, J. M., and McCulloch, A. D., 1993, "Mechanics of active contraction in cardiac muscle: Part I—constitutive relations for fiber stress that describe deactivation," *ASME J. Biomech. Eng.*, **115**, pp. 72–81.
- [9] Tseng, W. Y., 2000, "Magnetic resonance imaging assessment of left ventricular function and wall motion," *J. Formos Med. Assoc.*, **99**, pp. 593–602.
- [10] Weiss, J. A., Rabbitt, R. D., and Bowden, A. E., 1998, "Incorporation of medical image data in finite element models to track strain in soft tissues," *Proc. SPIE*, **3254**, pp. 477–484.
- [11] Veress, A. I., Phatak, N., and Weiss, J. A., 2004, "Deformable image registration with hyperelastic warping," in *The Handbook of Medical Image Analysis: Segmentation and Registration Models*, Marcel Dekker, Inc., NY.
- [12] Rabbitt, R. D., Weiss, J. A., Christensen, G. E., and Miller, M. I., 1995, "Mapping of hyperelastic deformable templates using the finite element method," *Proc. SPIE*, **2573**, pp. 252–265.
- [13] Veress, A. I., Weiss, J. A., Gullberg, G. T., Vince, D. G., and Rabbitt, R. D., 2003, "Strain measurement in coronary arteries using intravascular ultrasound and deformable images," *ASME J. Biomech. Eng.*, **124**, pp. 734–741.
- [14] Christensen, G. E., Rabbitt, R. D., and Miller, M. I., 1996, "Deformable templates using large deformation kinematics," *IEEE Trans. Image Process.*, **5**, pp. 1435–1447.
- [15] Marsden, J. E., and Hughes, T. J. R., 1994, *Mathematical Foundations of Elasticity*, Dover, Mineola, NY.
- [16] Simo, J. C., and Hughes, T. J. R., 1998, *Computational Inelasticity*, Springer, NY.
- [17] Bathe, K.-J., 1996, *Finite Element Procedures*, Prentice-Hall, Englewood Cliffs, NJ.
- [18] Bathe, K.-J., 1982, *Finite Element Procedures in Engineering Analysis*, Prentice-Hall, Englewood Cliffs, NJ.
- [19] Matthies, H., and Strang, G., 1979, "The solution of nonlinear finite element equations," *Int. J. Numer. Methods Eng.*, **14**, pp. 1613–1626.
- [20] Powell, M. J. D., 1969, *A Method for Nonlinear Constraints in Minimization Problems in Optimization*, Academic Press, NY.
- [21] Berne, R. M., and Levy, M. N., 1998, *Physiology*, Mosby Year Book, St. Louis, MO.
- [22] Spencer, A., 1980, *Continuum Mechanics*, Longman, NY.
- [23] Weiss, J., Maker, B., and Govindjee, S., 1996, "Finite element implementation of incompressible transversely isotropic hyperelasticity," *Comput. Methods Appl. Mech. Eng.*, **135**, pp. 107–128.
- [24] Humphrey, J. D., Strumpf, R. K., and Yin, F. C., 1990, "Determination of a constitutive relation for passive myocardium: II. Parameter estimation," *ASME J. Biomech. Eng.*, **112**, pp. 340–346.
- [25] Maker, B. N., Ferencz, R. M., and Hallquist, J. O., 1990, "NIKE3D: A nonlinear, implicit, three-dimensional finite element code for solid and structural mechanics," Lawrence Livermore National Laboratory Technical Report No. UCRL-MA #105268.
- [26] Huttenlocher, D. P., Klanderman, G. A., and Rucklidge, W. J., 1993, "Comparing images using the Hausdorff distance," *IEEE Trans. Pattern Anal. Mach. Intell.*, **15**, pp. 850–863.
- [27] Jiang, H., Holton, K. S., and Robb, R. A., 1992, "Image registration of multimodality 3-D medical images by chamfer matching," *Proc. SPIE*, **1660**, pp. 356–366.
- [28] Bland, J. M., and Altman, D. G., 1986, "Statistical methods for assessing agreement between two methods of clinical measurement," *Lancet*, **1**, pp. 307–310.
- [29] Humphrey, J. D., Strumpf, R. K., and Yin, F. C., 1990, "Determination of a constitutive relation for passive myocardium: I. A new functional form," *ASME J. Biomech. Eng.*, **112**, pp. 333–339.
- [30] Gonzalez, R. C., and Woods, R. E., 1992, *Digital Image Processing*, Addison-Wesley, Reading, MA.
- [31] Omens, J. H., Farr, D. D., McCulloch, A. D., and Waldman, L. K., 1996, "Comparison of two techniques for measuring two-dimensional strain in rat left ventricles," *Am. J. Physiol.*, **271**, pp. H1256–H1261.
- [32] Guccione, J. M., and McCulloch, A. D., 1993, "Mechanics of active contraction in cardiac muscle: Part II—constitutive relations for fiber stress that describe deactivation," *ASME J. Biomech. Eng.*, **115**, pp. 82–90.
- [33] Tseng, W. Y., Reese, T. G., Weisskoff, R. M., Brady, T. J., and Wedeen, V. J., 2000, "Myocardial fiber shortening in humans: Initial results of MR imaging," *Radiology*, **216**, pp. 128–139.
- [34] MacGowan, G. A., Shapiro, E. P., Azhari, H., Siu, C. O., Hees, P. S., Hutchins, G. M., Weiss, J. L., and Rademakers, F. E., 1997, "Noninvasive measurement of shortening in the fiber and cross-fiber directions in the normal human left ventricle and in idiopathic dilated cardiomyopathy," *Circulation*, **15**, pp. 535–541.
- [35] Schwartzman, P. R., Fuchs, F. D., Mello, A. G., Coli, M., Schwartzman, M., and Moreira, L. B., 2000, "Normal values of echocardiographic measurements. A population-based study," *Arq. Bras. Cardiol.*, **75**, pp. 111–114.
- [36] Miller, M. I., Trounev, A., and Younes, L., 2002, "On the metrics and Euler-Lagrange equations of computational anatomy," *Annu. Rev. Biomed. Eng.*, **4**, pp. 375–405.
- [37] Davatzikos, C., 1996, "Spatial normalization of 3D brain images using deformable models," *J. Comput. Assist. Tomogr.*, **20**, pp. 656–665.
- [38] Bajcsy, R., Lieberman, R., and Reivich, M., 1983, "A computerized system for the elastic matching of deformed radiographic images to idealized atlas images," *J. Comput. Assist. Tomogr.*, **7**, pp. 618–625.
- [39] Moshfeghi, M., 1994, "Three-dimensional elastic matching of volumes," *IEEE Trans. Image Process.*, **3**, pp. 128–138.
- [40] Gee, J., Reivich, M., and Bajcsy, R., 1993, "Elastically deforming 3D atlas to match anatomical brain images," *J. Comput. Assist. Tomogr.*, **17**, pp. 225–236.
- [41] Klein, G. J., Reutter, B. W., and Huesman, R. H., 1997, "Non-rigid summing of gated PET via optical flow," *IEEE Trans. Nucl. Sci.*, **44**, pp. 1509–1512.
- [42] Gilchrist, C. L., Xia, J. Q., Setton, L. A., and Hsu, E. W., 2004, "High-resolution determination of soft tissue deformations using MRI and first-order texture correlation," *IEEE Trans. Med. Imaging*, **23**, pp. 546–553.
- [43] Usyk, T. P., Mazhari, R., and McCulloch, A. D., 2000, "Effect of laminar orthotropic myofiber architecture on regional stress and strain in the canine left ventricle," *J. Elast.*, **61**, pp. 143–164.
- [44] Omens, J. H., May, K. D., and McCulloch, A. D., 1991, "Transmural distribution of three-dimensional strain in the isolated arrested canine left ventricle," *Am. J. Physiol.*, **261**, pp. H918–H928.
- [45] Costa, K. D., Holmes, J. W., and McCulloch, A. D., 2001, "Modeling cardiac mechanical properties in three dimensions," *Philos. Trans. R. Soc. London, Ser. A*, **359**, pp. 1233–1250.
- [46] Moulton, M. J., Creswell, L. L., Downing, S. W., Actis, R. L., Szabo, B. A., Vannier, M. W., and Pasque, M. K., 1996, "Spline surface interpolation for calculating 3-D ventricular strains from MRI tissue tagging," *Am. J. Physiol.*, **270**, pp. H281–H297.
- [47] Germano, G., Kiat, H., Kavanagh, P. B., Moriel, M., Mazzanti, M., Su, H. T., Van Train, K. F., and Berman, D. S., 1995, "Automatic quantification of ejection fraction from gated myocardial perfusion SPECT," *J. Nucl. Med.*, **36**, pp. 2138–2147.
- [48] Veress, A. I., Weiss, J. A., Klein, G. J., and Gullberg, G. T., 2002, "Quantification of 3D left ventricular deformation using hyperelastic warping: Comparisons between MRI and PET imaging," *Comput. Cardiol.*, pp. 709–712.
- [49] Picano, E., Lattanzi, F., Orlandini, A., Marini, C., and L'Abbate, A., 1991, "Stress echocardiography and the human factor: The importance of being expert," *J. Am. Coll. Cardiol.*, **17**, pp. 666–669.
- [50] Cohn, J. N., Johnson, G., Ziesche, S., Cobb, F., Francis, G., Tristani, F., Smith, R., Dunkman, W. B., Loeb, H., and Wong, M., 1991, "A comparison of enalapril with hydralazine-isosorbide dinitrate in the treatment of chronic congestive heart failure," *N. Engl. J. Med.*, **325**, pp. 303–310.
- [51] Zerhouni, E. A., Parish, D. M., Rogers, W. J., Yang, A., and Shapiro, E. P., 1988, "Human heart: Tagging with MR imaging—A method for noninvasive assessment of myocardial motion," *Radiology*, **169**, pp. 59–63.
- [52] Axel, L., Goncalves, R. C., and Bloomgarden, D., 1992, "Regional heart wall motion: Two-dimensional analysis and functional imaging with MR imaging," *Radiology*, **183**, pp. 745–750.
- [53] McVeigh, E. R., and Atalar, E., 1992, "Cardiac tagging with breath-hold cine MRI," *Magn. Reson. Imaging*, **28**, pp. 318–327.
- [54] Ungacta, F. F., Davila-Roman, V. G., Moulton, M. J., Cupps, B. P., Moustakidis, P., Fishman, D. S., Actis, R., Szabo, B. A., Li, D., Kouchoukos, N. T., and Pasque, M. K., 1998, "MRI-radiofrequency tissue tagging in patients with aortic insufficiency before and after operation," *Ann. Thorac. Surg.*, **65**, pp. 943–950.
- [55] Buchalter, M. B., Weiss, J. L., Rogers, W. J., Zerhouni, E. A., Weisfeldt, M. L., Beyar, R., and Shapiro, E. P., 1990, "Noninvasive quantification of left ventricular rotational deformation in normal humans using magnetic resonance imaging myocardial tagging," *Circulation*, **81**, pp. 1236–1244.
- [56] Ozturk, C., and McVeigh, E. R., 2000, "Four-dimensional B-spline based motion analysis of tagged MR images: Introduction and in vivo validation," *Phys. Med. Biol.*, **45**, pp. 1683–1702.
- [57] Atalar, E., and McVeigh, E., 1994, "Optimum tag thickness for the measurement of motion by MRI," *IEEE Trans. Med. Imaging*, **13**, pp. 152–160.

- [58] Tseng, W. Y., Wedeen, V. J., Reese, T. G., Smith, R. N., and Halpern, E. F., 2003, "Diffusion tensor MRI of myocardial fibers and sheets: Correspondence with visible cutface texture," *J. Magn. Reson. Imaging*, **17**, pp. 31–42.
- [59] Tseng, W. Y. I., Reese, T. G., Weisskoff, R. M., Brady, T. J., Dinsmore, R. E., and Wedeen, V. J., 1997, "Mapping myocardial fiber and sheet function in humans by magnetic resonance imaging (MRI)," *Circulation, Suppl. S*, **96**, pp. 1096.
- [60] Humphrey, J. D., 2002, *Cardiovascular Solid Mechanics: Cells, Tissues and Organs*, Springer-Verlag, NY.
- [61] Costa, K. D., May-Newman, K., Farr, D. D., O'Dell, W. G., McCulloch, A. D., and Omens, J. H., 1997, "Three-dimensional residual strain in midanterior canine left ventricle," *Am. J. Physiol.*, **273**, pp. H1968–H1976.
- [62] Weiss, J. A., Gardiner, J. C., and Bonifasi-Lista, C., 2002, "Ligament material behavior is nonlinear, viscoelastic and rate- independent under shear loading," *J. Biomech.*, **35**, pp. 943–950.
- [63] Young, A. A., Kraitchman, D. L., Dougherty, L., and Axel, L., 1995, "Tracking and finite element analysis of stripe deformation in magnetic resonance tagging," *IEEE Trans. Med. Imaging*, **14**, pp. 413–421.
- [64] Guccione, J. M., McCulloch, A. D., and Waldman, L. K., 1991, "Passive material properties of intact ventricular myocardium determined from a cylindrical model," *ASME J. Biomech. Eng.*, **113**, pp. 42–55.